Correspondence to:
M. Haseloff,
marianne.haseloff@earth.ox.ac.uk

Englacial Pore Water Localizes Shear in Temperate Ice Stream Margins

M. Haseloff[1,2] , **I. J. Hewitt[2]** , and **R. F. Katz[1]**

[1]Department of Earth Sciences, University of Oxford, Oxford, UK, [2]Mathematical Institute, University of Oxford, Oxford, UK

Abstract The margins of fast-moving ice streams are characterized by steep velocity gradients. Some of these gradients cannot be explained by a temperature-dependent viscosity alone. Laboratory data suggest that water in the ice-grain matrix decreases the ice viscosity; we propose that this causes the strong localization of shear in temperate ice stream margins. However, the magnitude of weakening and its consequences for ice stream dynamics are poorly understood. Here we investigate how the coupling between temperate ice properties, ice mechanics, and drainage of melt water from the ice stream margin alters the dynamics of ice streams. We consider the steady-state ice flow, temperature, water content, and subglacial water drainage in an ice stream cross section. Temperate ice dynamics are modeled as a two-phase flow, with gravity-driven water transport in the pores of a viscously compacting and deforming ice matrix. We find that the dependence of ice viscosity on meltwater content focuses the temperate ice region and steepens the velocity gradients in the ice stream margin. It provides a possible explanation for the steep velocity gradients observed in some ice stream shear margins. This localizes heat dissipation there, which in turn increases the amount of meltwater delivered to the ice stream bed. This process is controlled by the permeability of the temperate ice and the sensitivity of ice viscosity to meltwater content, both of which are poorly constrained properties.

1. Introduction

Ice stream shear margins mark the transition from the fast flow of an ice stream to the slow flow of neighboring ice ridges. This transition occurs over a distance of a few ice thicknesses, as seen, for example, in Figure 1. This leads to high strain rates and intense heat dissipation (Echelmeyer et al., 1994; Raymond, 1996; Schoof, 2004) and can cause the formation of temperate ice (Haseloff et al., 2015, 2018; Jacobson & Raymond, 1998; Meyer & Minchew, 2018; Schoof, 2012; Suckale et al., 2014). Further addition of dissipated heat to the temperate ice leads to melting within the ice matrix.

The fast sliding of ice streams is enabled by water at the bed, which weakens the ice stream bed and/or promotes slip at the ice-bed contact. The water content of the bed is controlled by the basal energy balance—in particular, by a competition between basal heat dissipation, geothermal heating, and conductive cooling (e.g., Beem et al., 2010; Christoffersen et al., 2014; Raymond, 2000). In the presence of temperate ice, we expect this energy balance to be altered in two ways: directly by the addition of meltwater draining from the temperate ice region to the bed and indirectly through thermo-mechanical coupling between the meltwater content of the marginal ice and enhanced ice deformation. In this study, we investigate how these processes change the steady-state flow and the production and distribution of meltwater.

Recent progress in the theory of temperate ice physics (Aschwanden et al., 2012; Hewitt & Schoof, 2017; Schoof & Hewitt, 2016) provides a framework to describe gravity-driven percolation of meltwater through the temperate ice matrix. However, there are few experimental measurements of the physical properties that control the system. Some data show that the viscosity of ice decreases sharply with meltwater content in the ice (Duval, 1977), but these experiments remain unrepeated and cover only a small part of the expected range of meltwater content within an ice sheet. Very little experimental data exist to constrain the permeability of temperate ice, which controls how fast meltwater drains from the ice, or the compaction viscosity of ice (also referred to as bulk viscosity), which controls the resistance of the ice matrix to compaction. Therefore, we study the sensitivity of ice stream dynamics to these properties over a broad range of values.

The extent of the temperate ice region in a shear margin depends on the mechanics of the transition between fast and slow moving ice; different models have been proposed to describe this transition. Common to all
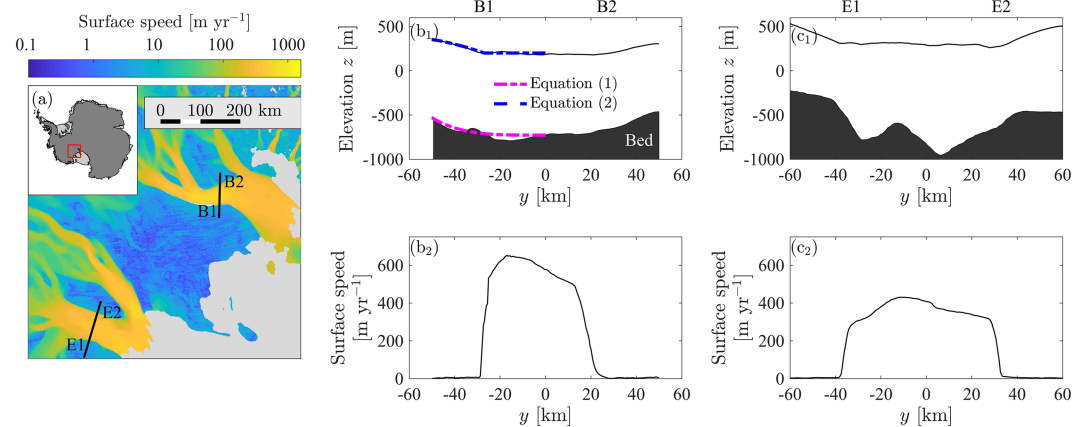
Figure 1. Examples of ice stream profiles. Panel a shows velocity map of the Siple Coast, with the location of the two profiles in panels b and c marked with black lines. Gray shading indicates the Ross ice shelf. Panel b_1 shows surface elevation and bed across Whillans ice stream, and panel b_2 shows the surface velocity across the same profile. Panel c_1 shows surface elevation and bed across MacAyeal ice stream, and panel c_2 shows the surface velocity across the same profile. The parameter values used to obtain the fitted surface and bed profile in panel b_1 are listed in Table 1. Figure generated with Antarctic Mapping Tools and Quantarctica (Greene et al., 2017; Matsuoka et al., 2018) with velocity data from Rignot et al. (2011, 2017) and bed/surface elevation data from Fretwell et al. (2013).

of these models is the assumption that this transition is related to a change in basal yield stress. Subglacial sediments underlying ice streams deform plastically (Tulaczyk et al., 2000a), and hence, slip is possible only when the basal shear stress reaches the yield stress of the bed τ_c.

Models linking the basal yield stress to physical processes can be divided into two categories. In the first, τ_c is a function of temperature, in which case the transition from slip to no slip is linked to a transition from a temperate to a frozen bed (Haseloff et al., 2015, 2018; Jacobson & Raymond, 1998; Schoof, 2012). In the second, τ_c is a function of the water pressure in the subglacial sediment, in which case the transition from slip to no slip is hydrologically controlled (Elsworth & Suckale, 2016; Kyrke-Smith et al., 2014, 2015; Meyer et al., 2018; Perol et al., 2015; Platt et al., 2016).

The basal yield stress can be linked to the water pressure in the bed through a relationship of the form $\tau_c(N)$ with $\partial \tau_c/\partial N > 0$ where the effective pressure N is the difference between the normal stress at the bed and the water pressure (e.g., Tulaczyk et al., 2000a; Bougamont et al., 2003). One mechanism proposed to strengthen the bed invokes subglacial channels in ice stream shear margins (Elsworth & Suckale, 2016; Meyer et al., 2018; Perol et al., 2015; Platt et al., 2016). These channels operate at low water pressure and draw in water from the surrounding bed. This increases the effective pressure N locally around the channel, which leads to a strengthening of the bed there.

Less attention has been given to a second hydrological mechanism by which the bed can be locally strengthened: Many ice streams flow in topographic lows and are bordered by ice ridges. Two examples of this behavior are shown in Figure 1. An increase in bed elevation and/or surface elevation causes an increase in effective pressure and hence an increase in bed strength, promoting a transition from yielded to unyielded bed. This is a simplified description of the mechanism that stabilizes ice stream margins in the numerical simulations of Kyrke-Smith et al. (2014, 2015). Observations show that both ice ridges and bed troughs are present in parts of the Siple Coast (Fretwell et al., 2013).

Our goal is to investigate the effect of temperate ice physics on ice stream dynamics. We focus on ridge-/topography-controlled shear margins by coupling a thermo-mechanical model for an ice stream cross section to a simple hydrological model, and to a model for temperate ice. The rheology of the temperate ice accounts for weakening due to meltwater in the ice matrix. The model is described in section 2. In section 3 we demonstrate that the coupling between the temperate ice physics and the viscosity of ice leads to a strong localization of shear in temperate ice stream margins and an enhanced meltwater flow from the ice to the bed. We discuss our results in section 4.
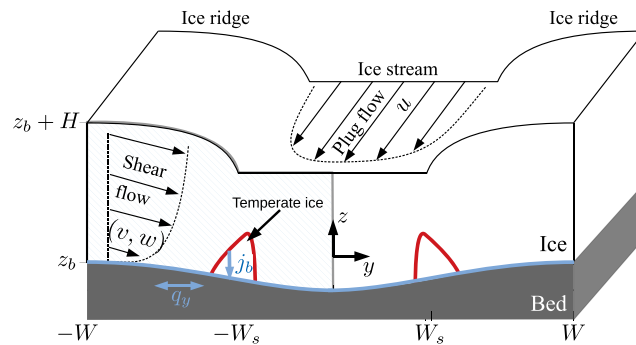
Figure 2. Sketch of the model geometry. We consider an ice stream of width $2W_s$ bordered by ridges of width $2(W - W_s)$. The bed elevation is z_b, and the ice thickness is H. We assume symmetry about the ice stream and ridge centers, so that we only need to model processes in the hatched area.

2. The Model

We use a simplified model setup that captures the main aspects of the ice stream cross sections shown in Figure 1, without attempting to directly fit observations. Specifically, we consider an ice stream bordered by ice ridges on both sides, as in Figure 2. The x coordinate is aligned with the principal direction of ice stream flow, y is in the lateral direction, and z points vertically upward. We assume mirror symmetry about the ice ridge and ice stream centers, and we locate the ice stream center at $y = 0$ and the ice ridge centers at $y = \pm W$. The ice stream shear margin, the transition between ice stream and ice ridge, is at $y = \pm W_s$. Consequently, the ice stream has width $2W_s$, and the ice ridge width is $2(W - W_s)$.

Gradients in the downstream direction ($\partial/\partial x$) are generally smaller than in the lateral and vertical directions, and therefore, we neglect or parametrize these. We obtain an essentially two-dimensional model that only considers processes in y-z plane. If we also neglect advection and lateral diffusion of heat, as we will do for most of this study, we can further reduce the model to a quasi-one-dimensional, depth-integrated model in the across-stream (y) direction. While this model reduction allows us to focus on the relevant physical processes, neglecting lateral advection might substantially alter the extent of the temperate ice region, particularly in the presence of ice ridges (Haseloff et al., 2018; Jacobson & Raymond, 1998; Suckale et al., 2014).

Table 1

Top: Geometric and Climatic Model Parameters, Obtained From a Fit of the Velocity and Ice Thickness Profile of the Shear Margin of Whillans Ice Stream, Marked with B1 in Figure 1

Description	Symbol	Value	Units
Accumulation rate	$\dot{a}$	0.05	m year^{-1}
Flow parameter	$\bar{A}_0$	2.5×10^{-25}	Pa^{-3} s^{-1}
Surface slope	$\sin \alpha$	10^{-3}	
Reference thickness of ice stream	H_c	927.6	m[a]
Geothermal heat flux	q_{geo}	70×10^{-3}	W m^{-2}
Surface temperature	T_s	-26.5	° C
Reference center velocity of ice stream	u_c	650	m year^{-1}
Ice stream half width	W_s	27	km
Half width of model domain	W	50.3	km
Bed parameter	z_0	-727.6	m
Bed parameter	z_4	200.9	m
Excess meltwater parameter	q_0		m s^{-1}
Hydrological potential in ice stream center	Φ_c		Pa

Note. The surface temperature T_s is taken from Alley and Bentley (1988). q_0 and Φ_c are free parameters in the model, determined from matching the boundary conditions (8) and (14).
[a]Note that in Figure 3 we use $H_c = 1{,}004$ m for Example 2 and $H_c = 827.2$ m for Example 3.

Table 2
Constants in the Model

Description	Symbol	Value	Units
Drainage parameter	a	3	
Dynamic viscosity of water	η_w	1.8×10^{-3}	Pa s
Heat capacity	c_p	2×10^3	J kg^{-1} K^{-1}
Acceleration due to gravity	g	9.81	m s^{-2}
Reference sediment thickness	h_w	1	m
Thermal conductivity	k	2.3	W m^{-1} K^{-1}
Hydraulic permeability of the sediment	k_d	between 10^{-19} and 10^{-13}	m^2
Permeability constant of temperate ice	k_w	between 10^{-12} and 10^{-8}	m^2
Latent heat of fusion	L_h	330×10^3	J kg^{-1}
Friction coefficient	μ	0.5	
Viscosity exponent	n	3	
Reference effective pressure	N_0	10^6	Pa
Permeability exponent	ν	between 2 and 3	
Gas constant	R	8.314	J mol^{-1} K^{-1}
Density of ice	ρ	910	kg m^{-3}
Density of water	ρ_w	1000	kg m^{-3}
Melting point temperature	T_m	273.15	K

Note. The values of the permeability constants k_w and ν are taken from Schoof and Hewitt (2016) but are largely uncertain. Values for hydraulic permeability of subglacial till k_d from Leeman et al. (2016).

In section 4 we therefore compare the temperature fields with and without advection. We present the reduced model here; the model with lateral and vertical advection of heat is described in Appendix B.

We are specifically interested in ice streams whose flow is affected by bed topography or the existence of an ice ridge. For the examples in this paper, we use a cross-stream bed profile

$$z_b = z_0 + z_4 \left(\frac{y}{W} \right)^4, \tag{1}$$

which we obtained by fitting the bed of Whillans Narrows across the shear margin marked as B1 in Figure 1. The parameters z_0, z_4, and W are listed in Table 1. The bed might additionally have a slope in the downstream direction, but it is not necessary to specify this.

Since we only model processes in the y-z plane, we cannot model the emergence of ice streams and ice ridges, as, for example, in Kyrke-Smith et al. (2014). Instead, we assume the existence of an ice stream and adopt the following approximate profile for the ice thickness H (Haseloff et al., 2015):

$$H + z_b = s_0 = \text{const.} \quad \text{for} \quad |y| \le W_s, \tag{2a}$$

$$-\frac{2}{n+2}(\rho g)^n \frac{\partial}{\partial y} \left(\bar{A}_0 H^{n+2} \left| \frac{\partial(H + z_b)}{\partial y} \right|^{n-1} \frac{\partial(H + z_b)}{\partial y} \right) = \dot{a} \quad \text{for} \quad W_s \le |y| \le W, \tag{2b}$$

with H ice thickness, ρ the density of ice, g the acceleration due to gravity, n the viscosity exponent in Glen's flow law, $\bar{A}_0$ the flow parameter of ice, and $\dot{a}$ the accumulation rate. We list the values of model constants in Table 2.

Equation (2a) describes an ice stream that is flat in the across-stream direction; that is, its surface elevation s_0 does not change with y (Haseloff et al., 2015). Equation (2b) is a standard shallow ice profile and is the appropriate equation for a steady-state ice ridge losing its mass to an ice stream (Haseloff et al., 2015; Hutter, 1983; Morland & Johnson, 1980). The boundary conditions are continuity of ice thickness across the ice stream shear margin and symmetry about the ice ridge center:

$$H + z_b = s_0 \quad \text{at} |y| = W_s \quad \text{and} \quad \frac{\partial(H + z_b)}{\partial y} = 0 \quad \text{at} |y| = W. \tag{3}$$

Our goal is to investigate the dependence of the ice stream dynamics on both temperature T and volumetric meltwater fraction ϕ. We take both of these effects into account by using (Cuffey & Paterson, 2010; Duval, 1977)

$$A(T, \phi) = A_m \begin{cases} \exp\left[-\frac{Q_c}{R}\left(\frac{1}{T} - \frac{1}{T_m}\right)\right] & \text{if} \quad T \leq T_m, \quad \phi = 0 \\ 1 + 235\phi & \text{if} \quad T = T_m, \quad \phi > 0 \end{cases}, \tag{4}$$

with $A_m = 2.47 \times 10^{-24}$ Pa^{-3} s^{-1}, R the gas constant, ϕ the meltwater fraction (or equivalently porosity), and

$$Q_c = \begin{cases} 60 \times 10^3 \text{J mol}^{-1} & \text{if } T < 263\text{K} \\ 115 \times 10^3 \text{J mol}^{-1} & \text{if } T \geq 263\text{K}. \end{cases} \tag{5}$$

The values for cold ice ($\phi = 0$) are based on the recommendations by Cuffey and Paterson (2010) Chapter 3, where we ignore the pressure dependence of the melting point. For temperate ice, we adapt the linear fit of the data by Duval (1977) given in Cuffey and Paterson (2010) Chapter 3, which recommends $A = A_m \times (1.3 + 235\phi)$ Pa^{-3} s^{-1}. By changing the intercept to A_m, we ensure that A is a continuous function of T and ϕ. Note, however, that this likely underestimates the water-softening effects of temperate ice described in section 3; we take (4) as a conservative estimate.

2.1. Ice Flow

We consider ice streams sliding along a bed with yield stress τ_c. In this case, the downstream velocity u in the x direction can be described by a typical "shallow" ice stream formulation (Haseloff et al., 2015; MacAyeal, 1989; Muszynski & Birchfield, 1987; Schoof, 2006):

$$\frac{\partial}{\partial y}\left(\eta H \frac{\partial u}{\partial y}\right) - \tau_c = -\rho g H \sin\alpha \qquad \text{if} \quad |y| < W_m, \tag{6a}$$

$$u = 0 \qquad \text{if} \quad |y| \geq W_m. \tag{6b}$$

η is the vertically averaged viscosity, which depends on the strain rate and the flow parameter of ice:

$$\eta = \frac{\overline{A^{-1/n}}}{2^{1/n}}\left|\frac{\partial u}{\partial y}\right|^{1/n-1}, \tag{7}$$

with $\overline{A^{-1/n}} = H^{-1}\int_{z_b}^{H+z_b} A^{-1/n}\mathrm{d}z$. The surface slope of the ice stream in downstream direction is given by the angle α.

The location W_m where slip goes to zero is not known a priori and must be determined as part of the solution. We assume a plastic rheology of the bed; that is, the bed yields and sliding occurs when the basal shear stress equals the yield stress of the bed (Tulaczyk et al., 2000a). In a depth-integrated model, this leads to the boundary conditions

$$\frac{\partial u}{\partial y} = 0 \quad \text{at} y = 0, \qquad u = \frac{\partial u}{\partial y} = 0 \quad \text{at} |y| = W_m. \tag{8}$$

Note that the position W_m where the speed goes to zero does not exactly coincide with the position where the ice ridge geometry transitions to the ice stream geometry (i.e., $W_m > W_s$).

The basal yield stress τ_c depends on the water pressure p_w in the bed through the effective pressure $N = \rho g H - p_w$ (Tulaczyk et al., 2000b):

$$\tau_c = \mu N = \mu\left(\rho g H - p_w\right), \tag{9}$$

with μ a friction coefficient (Tulaczyk et al., 2000a). To determine τ_c, we need a model for p_w or, equivalently, for N that we obtain next by considering subglacial water transport.

2.2. Subglacial Water Transport

Water transport along the bed is described by an equation for conservation of mass (e.g., Flowers, 2015):

$$\frac{\partial q_x}{\partial x} + \frac{\partial q_y}{\partial y} = \dot{m}_b + j_b, \tag{10}$$

with $\mathbf{q} = (q_x, q_y)$ the subglacial water flux (in m² s⁻¹), $\dot{m}_b$ the basal melt rate (in m s⁻¹), and j_b the water flux entering the bed from the temperate ice (in m s⁻¹).

Many different formulations for the subglacial drainage system are possible, which provide the necessary conditions to link $\mathbf{q}$ to the water content of the bed (e.g., Elsworth & Suckale, 2016; Hewitt, 2011; Lingle & Brown, 1987; Walder & Fowler, 1994). Models typically fall in two categories: distributed systems (Alley, 1989; Alley et al., 1986; Lliboutry, 1968; Walder, 1986; Walder & Fowler, 1994) and channelized systems (Nye, 1976; Röthlisberger, 1972). We aim to keep our model as simple as possible, and we therefore assume a distributed system following a Darcy-style flux law with transmissivity depending on effective pressure,

$$q_y = -\frac{k_d h_w}{\eta_w}\left(\frac{N_0}{N}\right)^a \frac{\partial \Phi}{\partial y}, \tag{11}$$

where

$$\Phi = \rho_w g z_b - N + \rho g H \tag{12}$$

is the hydraulic potential, k_d the permeability, h_w a reference sediment thickness, η_w the dynamic viscosity of water, N_0 a reference effective pressure, and $a > 0$. For $a = 3$ this is qualitatively similar to the model for flow through canals incised into the subglacial sediment derived by Walder and Fowler (1994). A similar dependence of transmissivity on effective pressure is obtained if we (reasonably) assume permeability is related to void fraction and use the relationship between void fraction and effective pressure found by Tulaczyk et al. (2000a). We can thus understand (10)–(12) as a weakly drained model for till, which allows both storage and drainage of water in the subglacial till layer.

We show below that observed bed permeabilities effectively correspond to the limit of an infinitely permeable bed. In this limit, (11) requires that the hydrological potential is constant (i.e., $\Phi = \Phi_c$ =const.), and the effective pressure becomes a function of the ice stream geometry only:

$$N = \rho_w g z_b + \rho g H - \Phi_c \qquad \text{for} \quad k_d \to \infty.$$

This illustrates how the existence of ice ridges and bed troughs can lead to a strengthening of the bed through the dependence of the basal yield stress on the effective pressure.

As we are not resolving the downstream coordinate, we approximate the downstream flux divergence $\partial q_x / \partial x$ by

$$\frac{\partial q_x}{\partial x} \approx -q_0 \left(\frac{N_0}{N}\right)^a, \tag{13}$$

with the constant q_0 determined as described below. In a model resolving variations in the downstream direction, this constant would depend on the downstream potential gradient. The dependence on N reflects the cross-stream variation of transmissivity, consistent with (11). Our symmetry conditions in the ice stream and ice ridge centers require that the lateral boundary conditions are

$$q_y = 0 \quad \text{at} \quad y = 0 \qquad \text{and} \qquad q_y = 0 \quad \text{at} \quad |y| = W. \tag{14}$$

The imposition of both of these conditions on (10) determines the constant q_0 (i.e., the downstream flux divergence must be such as to globally conserve mass). If $q_0 > 0$, an abundance of meltwater is produced across the ice stream, and it drains downstream. Conversely, if $q_0 < 0$, water must be provided to the ice stream bed from other sources—for example, from upstream regions or from a groundwater reservoir (e.g., Christoffersen et al., 2014).

We also require models for the basal melt rate $\dot{m}_b$ and the water flux from the ice j_b. For the former, we follow Lingle and Brown (1987) and assume that the geothermal heat flux q_{geo}, basal heat dissipation $\tau_c u$, and conductive cooling $k \, \partial T / \partial z|^+$ contribute to the basal melt rate:

$$\dot{m}_b = \frac{1}{\rho_w L_h}\left(q_{\text{geo}} + \tau_c u + k \left.\frac{\partial T}{\partial z}\right|^+\right). \tag{15}$$

In the next section, we determine the water flux from the temperate ice j_b and the conductive heat flux into the ice $k \partial T / \partial z|^+$.

2.3. Energy Equation

Temperatures in the ice can either be below the melting point ($T < T_m$, "cold ice") with zero moisture content ($\phi = 0$), or at the melting point ($T = T_m$, "temperate ice") with potentially a nonzero moisture content ($\phi \geq 0$). In general, heat transport can be by advection and diffusion. However, neglecting advection and lateral diffusion, we can express steady-state energy conservation in cold ice by

$$-k\frac{\partial^2 T}{\partial z^2} = \psi \qquad \text{for } T \leq T_m, \ \phi = 0, \tag{16}$$

with k the thermal conductivity and ψ the heat dissipation in the ice, which is given by the depth-integrated mechanical model:

$$\psi = \overline{\frac{A^{-1/n}}{2^{1/n}}} \left|\frac{\partial u}{\partial y}\right|^{(1+n)/n}. \tag{17}$$

The atmospheric temperature provides the surface boundary condition for the heat equation (16):

$$T = T_s \qquad \text{at } z = H + z_b. \tag{18}$$

We assume that the base of the ice is temperate throughout, including the ice ridge bed. Temperate ice might form up to a height $H_{ct} < H$ above the bed. In this case, we require the temperature to be at the melting point at $z = H_{ct} + z_b$ with no heat flux across that boundary (see also Schoof & Hewitt, 2016). This leads to the boundary conditions

$$T = T_m \text{ at } z = z_b \quad \text{if } H_{ct} = 0, \tag{19a}$$

$$T = T_m \quad \text{and} \quad k\frac{\partial T}{\partial z} = 0 \quad \text{at } z = H_{ct} + z_b \text{ if } H_{ct} > 0 \tag{19b}$$

at the lower boundary of the cold ice, where the first case applies when there is no temperate ice immediately above the bed.

For given ψ, the model for ice temperatures (16)–(19) can be integrated straightforwardly, and we obtain (Greve, 1997; Meyer & Minchew, 2018)

$$T(y,z) = \begin{cases} T_s + (T_m - T_s)\dfrac{s-z}{H} + \dfrac{\psi}{2k}(s-z)(z-z_b) & \text{if} \quad H_{ct} = 0 \\[2mm] \left.\begin{array}{ll} T_s + \dfrac{\psi}{k}\left[\dfrac{1}{2}\left(s^2 - z^2\right) - (s-z)(H_{ct}+z_b)\right] & \text{for} \quad z > H_{ct} \\[2mm] T_m & \text{for} \quad z_b \leq z \leq H_{ct} \end{array}\right\} \text{if} \quad H_{ct} \geq 0 \end{cases}, \tag{20}$$

with

$$H_{ct} = \max\left[0, H - \sqrt{\frac{2k}{\psi}(T_m - T_s)}\right]. \tag{21}$$

If H, T_s, and ψ are assumed to be known, then the extent of the temperate region can be directly estimated from (21) (Meyer & Minchew, 2018).

In our model, ψ and hence H_{ct} depend on the transverse coordinate y. In the examples below that take the temperature dependence of the rate factor into account, ψ depends on T. For these solutions, we iterate between solutions of the mechanical and thermodynamic models until convergence is reached. Equation (20) also provides the conductive heat flux into the ice needed in the calculation of the basal melt rate (15),

$$k\frac{\partial T}{\partial z}\bigg|^+ = \begin{cases} -\dfrac{k(T_m - T_s)}{H} + \dfrac{\psi}{2}H & \text{if } H_{ct} = 0 \\[2mm] 0 & \text{if } H_{ct} \geq 0. \end{cases} \tag{22}$$

2.4. Water Transport in the Ice

In temperate regions, additional heat dissipation leads to the formation of meltwater. This meltwater can be transported along with the viscously compacting and deforming ice matrix and percolate through it (Fowler, 1984; McKenzie, 1984; Schoof & Hewitt, 2016). As before, we neglect advection and assume that the relative moisture flux **j** in the ice is dominantly in the direction of gravity. Then the equations for mass and energy conservation for the ice-water mixture can be simplified to

$$\rho_w L_h \frac{\partial j_z}{\partial z} = \psi \qquad \text{for } T = T_m, \ \phi \geq 0, \tag{23a}$$

where L_h is the latent heat and j_z is the vertical relative moisture flux. At the cold-temperate boundary, we have no moisture flux, giving rise to the boundary condition

$$j_z = 0 \qquad \text{at } z = z_b + H_{ct}. \tag{23b}$$

Again, for a given rate factor, it is straightforward to integrate (23a)–(23b), yielding

$$j_z = -(H_{ct} + z_b - z)\frac{\psi}{\rho_w L_h} \quad \text{for } z_b \leq z \leq H_{ct}. \tag{24}$$

Note that the moisture flux is negative: Water flows in the negative z direction toward the bed. Consequently, the temperate ice contribution of water to the basal energy balance is $j_b = -j_z(y, z_b)$:

$$j_b(y) = H_{ct}\frac{\psi}{\rho_w L_h}. \tag{25}$$

Notably, in steady state we can calculate this contribution without knowledge of properties of the temperate ice region—in particular, without knowledge of the distribution of meltwater fraction ϕ and permeability k_ϕ within the ice. However, our goal is to investigate how moisture content affects ice stream dynamics, which requires us to turn to a model for moisture transport in the temperate ice.

We assume that water transport obeys Darcy's law:

$$j_z = \frac{k_\phi}{\eta_w}\left[-(\rho_w - \rho)g + \frac{\partial p_e}{\partial z}\right], \tag{26a}$$

with k_ϕ the permeability of the temperate ice region, η_w the dynamic viscosity of water, and g the acceleration due to gravity. Knowing j_z from (24), equation (26a) allows us to determine either the moisture content ϕ or the effective pressure p_e in the ice, provided we know the other quantity. p_e is the difference between ice pressure (which is cryostatic) and water pressure in the ice ($p_e = \rho g H - p_w$). The first term in the brackets of equation (26b) accounts for gravity-driven transport; the second accounts for transport due to pressure gradients. Nonzero effective pressures in the temperate ice lead to compaction, described by the relationship (Schoof & Hewitt, 2016)

$$p_e = \zeta_\phi \frac{\partial j_z}{\partial z}, \tag{26b}$$

with ζ_ϕ the compaction viscosity. At the bed, the effective pressure in the ice is set by the effective pressure in the bed:

$$p_e = N \quad \text{at } z = z_b \quad \text{if} \quad H_{ct} > 0. \tag{27}$$

In equations (26a) and (26b) we have introduced two quantities that depend on the moisture content of the ice: the permeability k_ϕ and the bulk viscosity ζ_ϕ. Both are poorly constrained by experimental data, so we draw on knowledge of related polycrystalline materials in Earth's mantle. These suggest a relationship of the form $k_\phi \propto \phi^\nu$, with $2 \leq \nu \leq 3$ (e.g., Rudge, 2018). In the absence of an empirical parametrization, we follow the models by Nye and Frank (1973) and Hewitt and Schoof (2017) and assume

$$k_\phi = k_w \phi^2. \tag{28}$$

Note that there is significant uncertainty about the correct value of k_w (as well as ν), with values in the literature ranging from $k_w = 10^{-12}$ m^2 (Hewitt & Schoof, 2017) to $k_w = 5 \times 10^{-8}$ m^2 (Nye & Frank, 1973).

One direct laboratory measurement of the permeability of temperate ice found $k_\phi = 10^{-18}$ m^2 (Jordan & Stark, 2001), but it is not clear at which meltwater content this value was obtained. At $\phi = 0.1\%$ and using $k_\phi = k_w \phi^2$, this measurement would correspond to $k_w = 10^{-12}$ m^2, the lower limit of values considered here.

The bulk viscosity describes the resistance of ice to compaction, and we expect less resistance with increasing meltwater fraction ($\partial \zeta_\phi / \partial \phi < 0$). Given that we have no empirical models for the compaction viscosity, we follow Schoof and Hewitt (2016) and use

$$\zeta_\phi = \zeta_0 \frac{\eta}{\phi}, \tag{29}$$

with ζ_0 a constant and η given by (7). We have confirmed that other models with a qualitatively similar behavior do not substantially alter our conclusions. Indeed, we find that ζ_ϕ is relatively unimportant.

To solve this model, we prescribe the geometry and the center velocity of the ice stream $u_c = u(y = 0)$ in addition to the model constants listed in Table 2. Equations (6)–(8) determine the across-stream velocity, equations (10)–(15) determine the subglacial melt rates and water fluxes, and (16)–(29) determine englacial temperatures and meltwater content. The center hydraulic potential $\Phi_c = \Phi(y = 0)$ (or equivalently the center effective pressure $N_c = N(y = 0)$) and the downstream flux constant q_0 are parameters to be determined as part of the solution. This is achieved by matching the lateral boundary conditions (8) and (14). Alternatively, we could fix (say) N_c, and the model would determine the centerline velocity u_c. We choose to fix the quantities that are readily observable and use the model to determine quantities that are unknown.

3. Results

In this section, we present solutions to the model outlined above. We start with solutions in the absence of thermo-mechanical coupling, assuming $A = \bar{A}_0 = $ constant (section 3.1). We then analyze the properties of the temperate ice region in detail (section 3.2) before considering the coupled system (section 3.3).

3.1. Ice Stream Dynamics Without Thermo-Mechanical Coupling

Without thermo-mechanical coupling, equations (2)–(25) can be solved independently of the temperate ice dynamics. We start by assuming an infinite permeability of the bed ($k_d = \infty$). This leads to a uniform hydrological potential ($\Phi = \Phi_c$) and requires the effective pressure to follow the shape of the ice thickness and basal topography (see equation (12)).

We solve (2)–(25) with Matlab ODE solvers. Solution of (2)–(25) with arbitrary choices of q_0 and Φ_c will generally not satisfy the lateral boundary conditions (8) and (14). We therefore use a Newton method to determine q_0 and Φ_c in such a way that the solutions of (2)–(25) satisfy these conditions.

To illustrate how the existence of ice ridges and/or topography leads to lateral confinement of ice streams, we solve three different, idealized versions of shear margin B1 of Whillans Narrows shown in Figure 1: one version with both topographic control and ice ridge (column 1 in Figure 3), one version with only the topographic control but no ice ridge (column 2 in Figure 3), and one version without topographic control, but with an ice ridge (column 3 in Figure 3). Rows a to f of Figure 3 show the temperature field, ice stream velocity u, effective pressure N, melt rate, downstream flux divergence $\partial q_x / \partial x$, and lateral water flux q_y. Black lines are solutions with an infinite permeability of the bed ($k_d = \infty$); magenta dotted lines in column 1 are solutions with a finite bed permeability ($k_d = 2.5 \times 10^{-18}$ m^2).

In all three examples, a laterally confined ice stream forms with no slip at its sides and fast slip in the center (Figures 3b$_1$ to 3b$_3$). This is as expected: The basal yield stress $\tau_c = \mu N$ (9) increases where the ice thickness and/or the bed elevation increase (see equation (12)), leading to a strengthening of the bed under the ridge and above the region of elevated basal topography. The rapidity of the transition from the fast velocity of the ice stream to the slow velocity of the ice ridge depends on the bed topography and ice geometry: The largest velocity gradients in the shear margin are attained for the example with only an ice ridge (column 3), while the example with only a topographic control has the smallest lateral velocity gradients (compare Figures 3b$_1$ to 3b$_3$).

Note that in the examples with an ice ridge (columns 1 and 3), the point $|y| = W_m$ where u goes to zero is distal to the point $|y| = W_s$ of the ice stream-ridge transition. For example, in column 3, we find $W_m = 29.4$ km, while we chose $W_s = 27$ km. This is a consequence of imposing the steady-state ice geometry; in a more
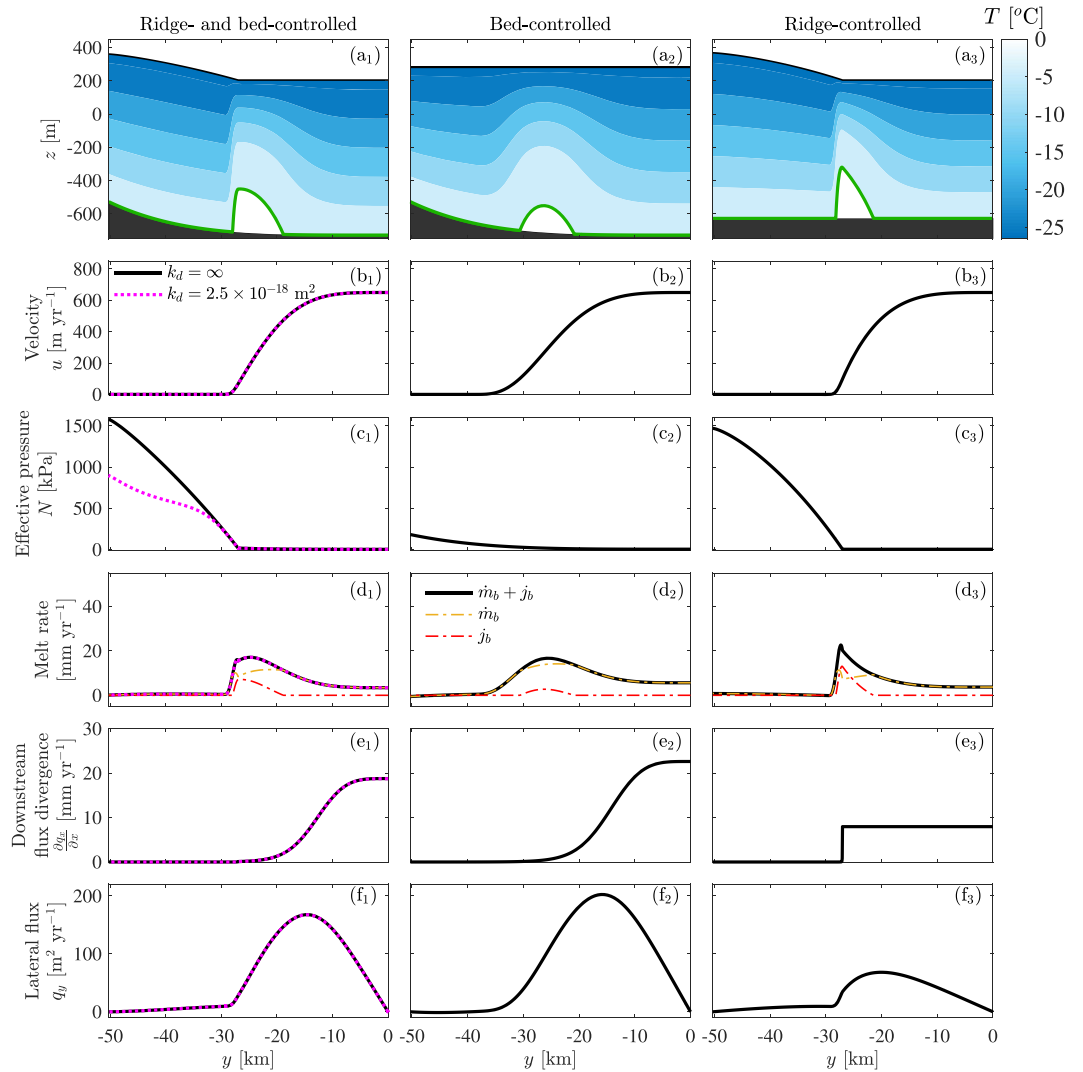
Figure 3. Example solution for the shear margin at Whillans narrows (marked as B1 in Figure 2) for a temperature- and meltwater-independent flow parameter $\bar{A}_0 = 2.5 \times 10^{-25}$ Pa^{-3} s^{-1}. Black lines show solutions for infinite hydraulic permeability ($k_d = \infty$); magenta dotted lines show solutions for finite hydraulic permeability ($k_d = 2.5 \times 10^{-18}$ m^2). Column 1 shows results with topographic control and ice ridge, column 2 shows results with only topographic control (using only (2a) instead of (2) with $H_c = 1,004$ m), column 3 shows results for ice ridge only (using $z_b = -627.2$ m instead of (1)). Row a shows temperature fields in the ice. The cold-temperate boundary is marked by a bold green line; gray shading indicates the bed. Row b shows velocity u, row c shows effective pressure N, row d shows melt rates (dashed red line: moisture flux from the ice j_b (25); dashed yellow line: melt rate at the bed $\dot{m}_b$ (15)), row e shows downstream flux divergence $\partial q_x / \partial x$, and row f shows lateral water flux q_y (a positive water flux is toward the center of the ice stream).

self-consistent model, we expect the ice thickness to adjust in response to changes in basal boundary conditions (see, e.g., Haseloff et al., 2018). In our model, the relative locations of W_m and W_s ensure that all the driving stress applied at the surface is balanced.

In the ice stream shear margin, where fast flow transitions to the stagnant ice ridge, a region of temperate ice forms (Figures 3a$_1$ to 3a$_3$). This is consistent with previous work (Haseloff et al., 2015, 2018; Jacobson & Raymond, 1998; Meyer & Minchew, 2018; Perol & Rice, 2015; Schoof, 2012; Suckale et al., 2014), even though the mechanism by which the ice stream shear margin is localized in these earlier studies differs from the mechanism considered here.

The shape and vertical extent of the temperate ice region depend on the way the shear margin is controlled. The purely bed-controlled shear margin has a wider, shallower temperate ice region (Figure 3a$_2$) in
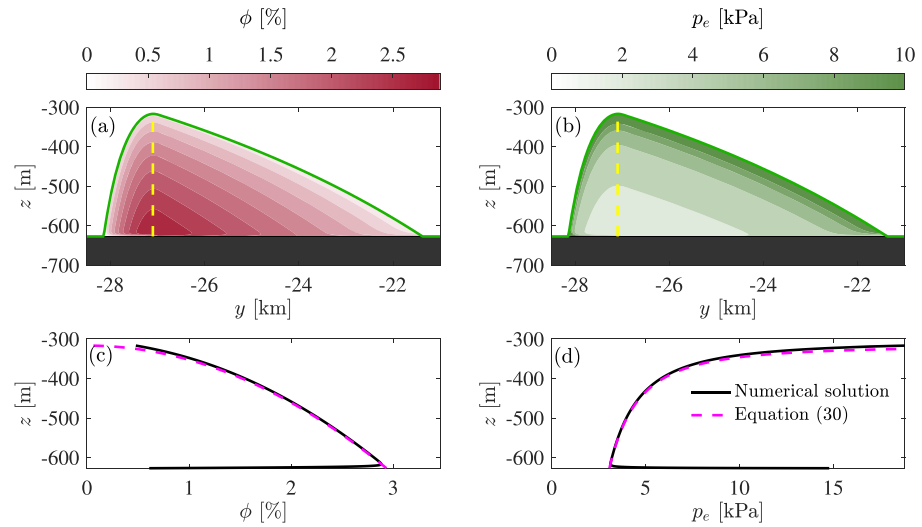
Figure 4. Sample solution of meltwater fraction and effective pressure in the temperate ice region for the ridge-controlled case in Figure 3 with a permeability constant $k_w = 10^{-12}$ m^2, other values as in Table 2. Panels a and b show meltwater fraction and effective pressure in the temperate ice region. The cold-temperate boundary is marked with the bold green line. Panels c and d show the meltwater fraction and effective pressure with height z at the point where the temperate ice region has its maximum vertical extent (broken yellow line in panels c and d).

comparison to the purely ridge-controlled shear margin (Figure 3a$_3$). The extent of the temperate ice region H_{ct} in (21) increases with increasing ψ (17). Heat dissipation in the bed-controlled case is less localized, which smooths out the temperate ice region.

Intuitively, we expect larger velocity gradients in the shear margin to also increase the water flux from the ice to the bed. That is confirmed by the results shown in Figures 3d$_1$ to 3d$_3$, which show the moisture flux from the ice j_b as a dashed red line, the melt rate at the bed $\dot{m}_b$ as a dashed yellow line, and the combined melt rate $\dot{m}_b + j_b$ as a solid black line. The moisture flux j_b is directly related to the height of the temperate ice region H_{ct} (see equation (25)); hence, the largest water flux is achieved in the ridge-controlled geometry.

The basal melt rate $\dot{m}_b$ is affected by heat dissipation in two ways: Heat dissipation in the ice itself reduces the amount of conductive cooling experienced at the bed (22), and heat dissipation along the ice-bed contact gives rise to the additional term $\tau_c u$. Naturally, where the ice velocity is zero, no heat is dissipated, and the basal melt rate is just the sum of geothermal heat flux q_{geo} and the conductive cooling $k\partial T/\partial z|^+ = k(T_m - T_s)/H$. Where temperate ice is present, there is no conductive cooling as $k\partial T/\partial z|^+ = 0$. Instead, the ice effectively provides a meltwater source term through j_b.

As most meltwater is produced in the shear margin, the subglacial water flow in the across-stream direction q_y is generally positive, that is, from the ice stream margin to the ice stream center (Figures 3f$_1$ to 3f$_3$). Under the ice ridge where there is no heat dissipation, the water flux is close to zero, as the conductive cooling term and the geothermal heat flux are almost matched.

The downstream flux divergence $\partial q_x/\partial x$ acts as an additional source or sink term in the energy balance. In contrast to the lateral water flux, $\partial q_x/\partial x$ reflects the effective pressure profiles through (13) (Figures 3e$_1$ to 3e$_3$). The effective pressure increases from the ice stream center to the ice ridge, and therefore, the downstream flux is largest in the ice stream center and almost zero under the ice ridge. In the three examples shown in Figure 3, the downstream flux divergence is positive, corresponding to excess meltwater being exported downstream.

Our solutions so far have assumed that the hydraulic permeability k_d of the bed is infinite. However, laboratory and field measurements find pressure-dependent bed permeabilities in the range 10^{-19} to 10^{-13} m^2 (Engelhardt et al., 1990; Leeman et al., 2016). To test the effect of a finite bed permeability, we use $k_d = 2.5 \times 10^{-18}$ m^2 and $N_0 = 1$ MPa, as reported for till samples from Whillans ice stream (Leeman et al., 2016). In our simple hydrological model, we find no discernible effect of having a finite bed permeability on the temperature and velocity fields (dotted magenta lines in Figures 3a$_1$ and 3b$_1$). The only noticeable effect of
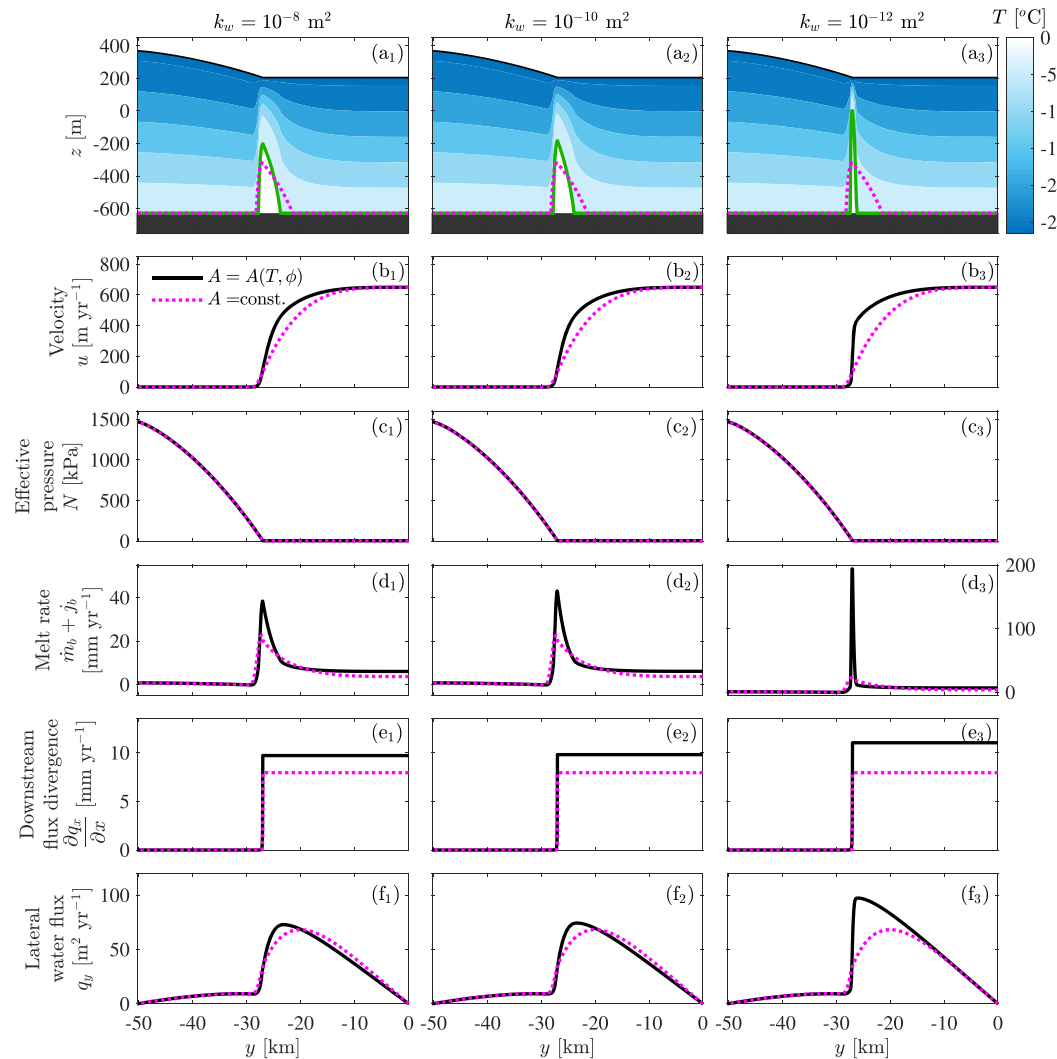
Figure 5. Effect of thermo-mechanical coupling for permeability parameter $k_w = 10^{-8}$ (column 1), $k_w = 10^{-10}$ m^2 (column 2), and $k_w = 10^{-12}$ m^2 (column 3). Same plotting scheme as in Figure 3 and same geometric parameters as in column 3 of Figure 3 (these solutions are plotted as dotted magenta lines). Note that the limits of the y axis of panel d$_3$ differ from those in panels d$_1$ and d$_2$.

a finite hydraulic permeability is a reduction of the effective pressure beneath the ice ridge, where the effective pressure now adjusts to maintain the subglacial water fluxes necessary to balance meltwater production (Figure 3c$_1$). Notably, the effective pressure is still smallest in the ice stream center, corresponding to a maximum in the downstream flux divergence there (Figure 3e$_1$). We conclude that taking the bed permeability to be effectively infinite is a reasonable assumption in the ice stream cross section (finite permeability may be important when considering downstream evolution).

3.2. Properties of the Temperate Ice Region

In the absence of thermo-mechanical coupling, the heat dissipation ψ, viscosity η, effective pressure N, and vertical extent of the temperate ice region H_{ct} can be determined from the solution of the depth-integrated model alone. Once these fields are known, the properties of the temperate ice region can be determined a posteriori from vertical integration of (26a)–(29).

Figures 4a and 4b show an example of the meltwater fraction and effective pressure in the ice for the ridge-controlled case, column 3 of Figure 3. For this example, we have assumed a permeability constant of $k_w = 10^{-12}$ m^2 and a viscosity constant of $\zeta_0 = 1$. The meltwater fraction (Figure 4a) increases gradually from the cold-temperate boundary (green line) toward the bed, up to a maximum value of about 3%.
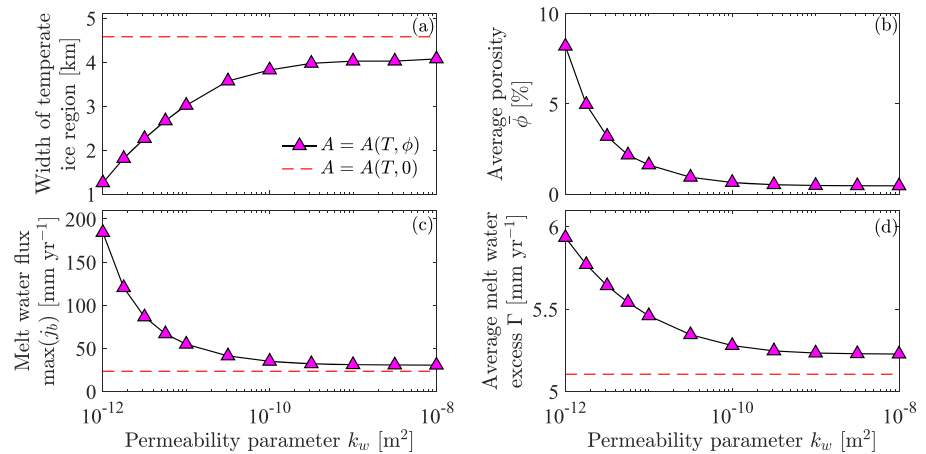
Figure 6. Maximum width of the temperate ice region (panel a), average porosities in the temperate ice at its maximum vertical extent (panel b), maximum meltwater flux from the temperate ice region j_b (panel c), and width-averaged excess meltwater production Γ (equation (31), panel d) as function of the temperate ice permeability parameter k_w. Dashed lines show the solution with no water dependence of the rate factor.

At the bed, a slender, low-porosity region forms. The effective pressure in the ice mirrors this behavior, in the sense that it decreases from the cold-temperate boundary toward the bed (Figure 4b), with a boundary layer forming at the bed to match the effective pressure in the subglacial system.

As can be shown by an asymptotic analysis (Appendix A and Schoof & Hewitt, 2016), the meltwater fraction and effective pressure in most of the temperate ice excluding the boundary layer at the bed and an additional boundary layer close to the cold-temperate boundary originate from a purely gravity-driven moisture flux (i.e., $\partial p_e / \partial z$ in equation (26a) can be neglected in this region). In other words, the negative buoyancy of the liquid is balanced by Darcy drag in the pores. This leads to the following expressions for meltwater fraction and effective pressure in the bulk of the temperate ice region:

$$\phi = \left(1 - \frac{z - z_b}{H_{\mathrm{ct}}}\right)^{1/2} \left(\frac{\psi H_{\mathrm{ct}}}{\rho_w L_h} \frac{\eta_w}{k_w(\rho_w - \rho)g}\right)^{1/2}, \qquad p_e = \frac{\psi}{\rho_w L_h} \frac{1}{\zeta_\phi} \tag{30}$$

(see magenta lines in Figures 4c and 4d). Note that in the literature on magma dynamics, this is the zero-compaction-length approximation (Spiegelman, 1993). For practical purposes, (30) means that the meltwater content of the temperate ice region is largely unaffected by the subglacial drainage system and the bulk viscosity. Instead, it is set by the permeability of the temperate ice and by the englacial heat dissipation. We next investigate the effect of coupling these two by allowing the viscosity to depend on the temperature and meltwater fraction in the ice.

3.3. Effect of Interstitial Meltwater Weakening

We model the effect of thermo-mechanical coupling by using the empirical fit (4), even though there is substantial uncertainty in the dependence of the rate factor on meltwater fraction ϕ in particular. We discuss these limitations in section 4. Results are shown in Figure 5 for the ridge-controlled example of Figure 3 for three different permeability constants k_w of the temperate ice, as indicated above each column.

The immediate effect of lowering the permeability constant k_w is a narrower temperate ice region with larger vertical extent (panels $5a_1$ to $5a_3$). This focussing is due to higher meltwater content in the temperate ice. A higher rate factor corresponds to weaker ice, and as the rate factor in the ice increases with increasing meltwater content, we also expect it to increase with decreasing permeability.

Heat dissipation in the ice is altered by two competing effects: It decreases with a lower viscosity (larger A) and increases with larger strain rates (see (17)). In warmer ice, strain rates in the ice increase because the weakening of ice in the shear margin promotes deformation there (see panels $5b_1-5b_3$; the dotted magenta lines show the velocity profile for a constant rate factor as in Figure 3). The net effect of lowering the temperate ice permeability is thus an increase in englacial heat dissipation, as can be seen from the melt rates shown in panels $5d_1-5d_3$. Note that the melt-rate axis in panel $5d_3$ is different. The sharp increase in local

heat dissipation leads to a slightly larger lateral water flux from the ice stream margin to its center (panels $5f_1$–$5f_3$) and an increase in the excess meltwater production (panels $5e_1$–$5e_3$).

We systematically investigate the dependence of these properties on the permeability constant k_w in Figure 6, which shows the width of the temperate ice region (Figure 6a), the average meltwater fraction in the temperate ice region (Figure 6b), the maximum meltwater flux from the temperate ice region (Figure 6c), and the average downstream water flux (Figure 6d) as functions of k_w. These quantities remain nearly constant for permeabilities larger than 10^{-9} m^2. In this limit (effectively the limit of $k_w \to \infty$), the permeability is large enough to drain nearly all meltwater from the temperate ice region, leading to average porosities of less than 0.5%. Note that the average meltwater fraction in the temperate ice does not go to exactly zero, as the slender boundary layers at the bottom and top of the temperate ice region have nonzero porosities even in the limit of large permeabilities. This explains the difference to the case where we only account for the temperature dependence of the viscosity (i.e., $A = A(T, \phi = 0)$, red dashed line in Figure 6).

For decreasing permeabilities, the average meltwater fraction in the temperate ice region increases up to approximately 8% for $k_w = 10^{-12}$ m^2. This explains the pronounced weakening we observe in the examples in Figure 5: At a meltwater fraction of 8%, equation (4) predicts a rate factor of $A = 4.89 \times 10^{-23}$ Pa^{-3} s^{-1}, which is 20 times larger than the rate factor for temperate ice with zero meltwater content.

The increase in meltwater production in the shear margin with decreasing temperate ice permeability (Figure 6c) does not only lead to a shift in the location of heat dissipation. It also increases the total amount of heat dissipated across the width of the ice stream, as is illustrated by the increase in the width-integrated downstream flux divergence Γ (Figure 6d),

$$\Gamma = \frac{1}{W} \int_{-W}^{0} \frac{\partial q_x}{\partial x} \mathrm{d}y = \frac{1}{W} \int_{-W}^{0} \left(\dot{m}_b + j_b \right) \mathrm{d}y, \tag{31}$$

which provides a measure for the excess meltwater production of the ice stream. Hence, we see a link between the global ice stream energy balance and the permeability of the temperate ice region, which is controlled by processes at the grain scale.

4. Discussion and Conclusions

We have investigated how the viscous coupling between the meltwater content of temperate ice and the ice mechanics alters the energy balance of ice streams. We find that the formation of temperate ice with a nonzero meltwater content weakens the ice locally and focuses lateral shear in the margin, consistent with observations of ice stream shear margins (Figure 1). This substantially increases heat dissipation there. This effect is an extension of the well-known weakening of ice in ice stream shear margins through the temperature-dependence of the viscosity (e.g., Suckale et al., 2014).

The most important consequence of this strain localization is an increase in the meltwater contribution from the temperate ice region to the basal meltwater budget. In the example of the Whillans-like margin considered here, this leads to an increase in average excess meltwater production of up to 14%. The magnitude of this effect is mainly controlled by the permeability of the temperate ice region and the water dependence of the viscosity.

The lack of a reliable physical model or empirical parametrization for the permeability of temperate ice introduces the largest source of uncertainty in our study. Existing models typically propose a relationship of the form $k_\phi = k_w \phi^2$ with values for k_w ranging from 10^{-12} to 5×10^{-8} m^2 (Hewitt & Schoof, 2017; Nye & Frank, 1973). Analogies of water flow in temperate ice to magma flow in the mantle suggest that the grain size plays a crucial role in controlling k_w. The value of $k_w = 5 \times 10^{-8}$ m^2 by Nye and Frank (1973) is based on a grain-size estimate of $d = 10^{-2}$ m, which is consistent with values found in some ice cores (Cuffey & Paterson, 2010). However, the high temperatures and strain rates in ice stream shear margins likely favor dynamic recrystallization processes, which produce smaller grain sizes. It is therefore conceivable that the permeability by Nye and Frank (1973) is an overestimate.

Our results indicate that the range of possible values of k_w from 10^{-12} to 10^{-8} m^2 suggested in the literature covers an extreme range of behaviors: At $k_w = 10^{-8}$ m^2 effectively all meltwater is drained immediately, leading to vanishing meltwater content in most of the temperate ice region (excluding narrow boundary layers at the top and bottom of the temperate ice region). In this limit, the effects of meltwater content on

ice stream dynamics are negligible. Conversely, for $k_w = 10^{-12}$ m^2, the average meltwater content of the temperate ice region is approximately 8%, far beyond the range of existing data for the rate factor $A(T, \phi)$ (Duval, 1977).

Further reduction of the englacial permeability coefficient k_w leads to further localization of the temperate ice region and higher porosities. This is unlikely to be realistic, and we expect lateral heat transport and the development of a more efficient englacial meltwater system (e.g., through a transition from a quadratic to a cubic dependence of the permeability on meltwater fraction Rudge, 2018) to eventually counteract continued localization.

In addition to uncertainties in the permeability of temperate ice, which controls the meltwater content directly, uncertainties in the dependence of the rate factor on the meltwater content also affect our results. Both the viscosity and the heat dissipation depend on the rate factor. Existing data for the dependence of the rate factor on the meltwater content is limited to porosities of less than 1%, but in our study we extrapolate a proposed linear relationship between the rate factor and the meltwater content to bulk porosities of 8%. It is likely that this relationship does not remain valid at such high porosities, but an assessment of the induced error is not possible without better experimental constraints on the rate factor. Additionally, there might be other processes affecting the development of viscosity of ice in ice stream margins. These include grain-size reduction, macroscopic damage, crystal fabric development, the existence of impurities, or a change in the strain-rate dependence of the viscosity (Goldsby & Kohlstedt, 2001; Minchew et al., 2018).

While the permeability and the rate factor of temperate ice are crucial in determining the role temperate ice plays in the ice stream energy balance, compaction of ice (through the bulk viscosity of ice) and the water content of the bed play only minor roles. Their impacts are confined to small boundary layers at the top and bottom of the temperate ice region. This implies that drainage of meltwater from the temperate ice region is well described by the balance of buoyancy and Darcy drag. This simplifies the solution of the underlying equations, as the dependence on the effective pressure in the ice can be neglected.

As the focus of our study is on the effect of interstitial meltwater weakening, we have chosen to represent subglacial hydrology in as simple a manner as possible, assuming a Darcy-style flux in the direction of gradients of the hydraulic potential with a transmissivity depending on effective pressure. However, observations suggests that complex drainage networks are likely to exist at ice stream beds (Blankenship et al., 1986, 1987; Engelhardt & Kamb, 1997; Gray et al., 2005; Fricker et al., 2007; Kamb, 2001), which our model cannot capture. In particular, as we only resolve the across-stream dimension, we cannot infer how the injection of substantial amounts of meltwater in the ice stream margin might affect the development of the subglacial drainage system in the downstream direction, for instance through the formation of a Röthlisberger channel (Elsworth & Suckale, 2016; Meyer et al., 2018; Perol et al., 2015; Röthlisberger, 1972). In our model effective pressure and downstream drainage are controlled by topography and ice geometry, rather than by the location of meltwater injection. This suggests that it is important to take these properties into account in studies of ice stream subglacial drainage.

We have neglected the effect of advection on the temperature field. However, the elevation difference between ridge and stream drives lateral inflow of cold ice into the ice stream. This may counteract the effect of shear heating and even lead to the elimination of the temperate region (Haseloff et al., 2018; Jacobson & Raymond, 1998; Suckale et al., 2014). Here, we investigate the magnitude of this effect for the ridge-controlled case shown in Figure 3$_3$.

One challenge of modeling lateral advection is that the calculation of the velocity field in the ice stream cross section requires modeling or parametrizing downstream advection of ice in the ice stream mass balance. If downstream transport is not accounted for, the ice stream thickens at a rate determined by the inflow of mass from the sides. This leads to an unrealistic upward motion of ice in the ice stream, skewing the temperature field.

In Appendix B, we present an analytical approximation for the in-plane velocity field without thermomechanical coupling (i.e., A =constant). To derive this approximation, we calculate the in-plane velocities from the "shallow" models underlying the assumed thickness profiles for the ice stream and ice ridge (2). This simple approximation cannot capture the narrow transition between these two flow regimes—this would require resolving the full Stokes flow (Haseloff et al., 2015). Instead, we linearly interpolate the velocities between W_m (the sliding onset) and W_s (the geometric stream-ridge boundary). The resulting velocity
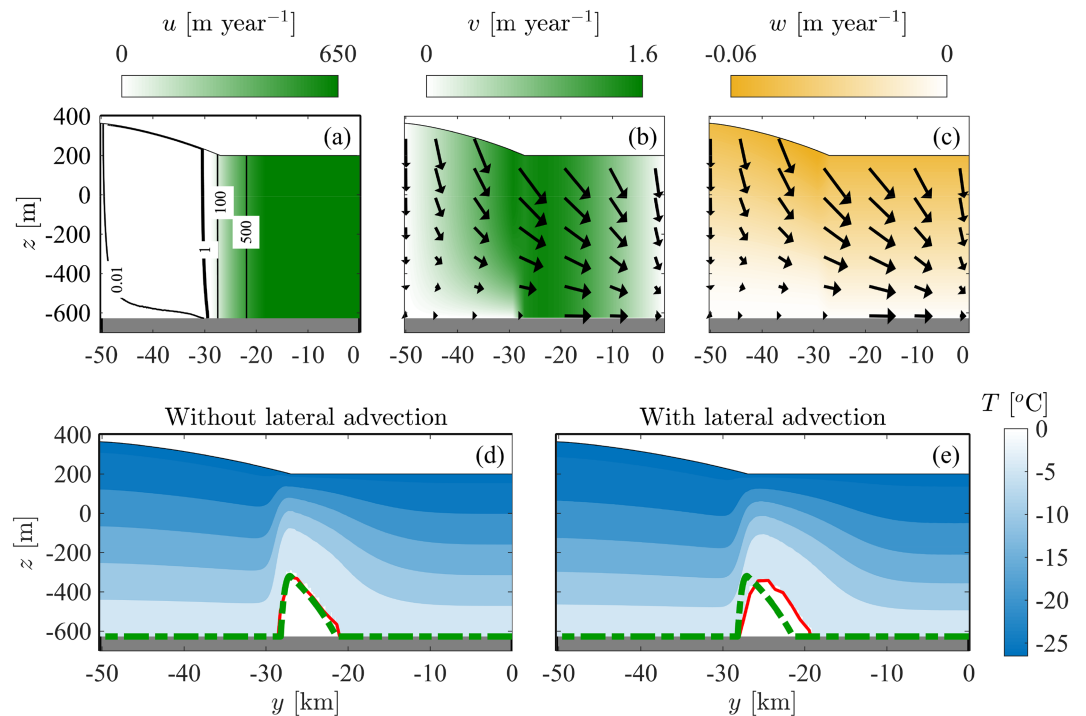
Figure 7. Effect of lateral advection of ice on temperate ice formation. Panel a: Downstream velocity is determined from solution of the two-dimensional Poisson's equation for u (B4). Panels b and c: In-plane velocities are from the analytical expressions (B7) and (B8) (see Appendix B for details). Panels d and e: Temperature fields are solutions of the two-dimensional heat equation (B1) with (d) and without (e) advection of ice. Red line: $T = 0$ contour from solution of extended heat equation (B1), green dashed line: $T = 0$ contour obtained from solution of (16).

fields are shown in Figures 7b and 7c. They are used to solve the two-dimensional heat equation (B1) with the finite-element solver Elmer/Ice (Gagliardini et al., 2013); see Figure 7e.

In the model with advection, the onset of the temperate ice region is slightly more gradual, and its maximum extent is shifted toward the ice stream (Figure 7e). Nevertheless, the change to the temperate ice region is subtle, suggesting that the weakening effects described above will be important in the presence of lateral advection of ice, too.

As well as in-plane advection terms, the solution to the full heat equation (B1) also includes lateral diffusion and a slight correction to the shear heating compared to our original model. The correction is due to vertical shear because the downstream velocity is now determined from solution of the two-dimensional Poisson's equation (B4); see Figure 7a. Including these terms is common in models for ice stream shear margins (e.g., Haseloff et al., 2015, 2018; Jacobson & Raymond, 1998; Suckale et al., 2014). To see the effect of these extra terms, we compare in Figure 7d the solutions to the heat equation (B1) for $v = w = 0$ with the simplified heat equation (16). There is reasonable agreement with the earlier model, which slightly underestimates the extent of the temperate ice region.

Several existing studies investigate the link between heat dissipation in ice stream shear margins and subglacial drainage in the absence of coupling between meltwater content of temperate ice and the viscosity of ice. Apart from taking into account this coupling, our approach differs from these studies by additionally accounting for the meltwater flux from the ice into the bed and by taking the lateral water flux into account (Beem et al., 2010; Christoffersen et al., 2014; Perol & Rice, 2015; Perol et al., 2015; Raymond, 2000). This allows us to investigate how the properties of the temperate ice region change the global energy balance of the ice stream.

Our approach also differs from existing studies through the mechanism that confines the ice stream flow: Instead of either prescribing a subglacial channel in the ice stream shear margin (Perol & Rice, 2015) or relying on the formation of a thermal boundary in ice stream margins (Haseloff et al., 2015, 2018; Schoof, 2012), we explicitly focus on ice streams that are hydrologically confined by their basal topography or by an

ice ridge (the latter also stabilize ice streams in Kyrke-Smith et al., 2014). Our results illustrate how each of these conditions in isolation, as well as in combination, is able to explain the existence of laterally confined ice stream flow. Both ice ridges and bed troughs are present in parts of the Siple Coast (Fretwell et al., 2013), though often in more complex forms than modeled here, as the example of MacAyeal ice stream in Figure 1c illustrates.

As is common for many studies of ice stream shear margins, we have focused on idealized, steady-state profiles. However, the dynamic history of the Siple Coast region is well documented (Catania et al., 2006, 2012; Conway et al., 2002; Fahnestock et al., 2000; Echelmeyer & Harrison, 1999; Hamilton et al., 1998; Hulbe & Fahnestock, 2007; Retzlaff & Bentley, 1993; Stephenson & Bindschadler, 1988; Stearns et al., 2005). Hence, we cannot expect to explain all observable properties of the Siple Coast velocity profiles. For example, it is conceivable that remnant temperate ice regions might explain the strong focussing seen in the margins of MacAyeal ice stream (see Figure 1). For this profile, the steady-state model presented here either predicts no temperate ice in the margin (when adapting the bed profile (1)) or predicts a much narrower ice stream with a temperate margin (using the observed bed profile across the margin marked as E2). This highlights the need to better understand the role of topography and the unsteady, three-dimensional dynamics not captured in our model.

Appendix A: Leading-Order Balance in the Temperate Ice Region

To understand the behavior of meltwater fraction and effective pressure in the temperate ice region, we assume a constant rate factor A and nondimensionalize equations (26a)–(27) by setting $p_e = N p_e^*$, $j = (\psi H_{ct})/(\rho_w L_h) j^*$, and $z = z_b + H_{ct} z^*$. Then the model can be written as

$$1 - z^* = \kappa \phi^\nu \left[1 - \alpha \frac{\partial p_e^*}{\partial z^*} \right], \qquad p_e^* = \beta \phi, \tag{A1}$$

with the boundary condition

$$p_e^* = 1 \qquad \text{at} z^* = 0 \tag{A2}$$

and the nondimensional location-dependent groups

$$\alpha(y) = \frac{N}{H_{ct}(\rho_w - \rho)g}, \qquad \beta(y) = \frac{\psi}{\rho_w L_h} \frac{1}{N \zeta_0 \eta}, \qquad \kappa(y) = \frac{\rho_w L_h}{\psi H_{ct}} \frac{k_0}{\eta_w}(\rho_w - \rho)g.$$

Typical values of the parameters can be estimated from the solutions of the model without thermo-mechanical coupling, which gives

$$10^{-2} \lesssim \alpha \lesssim 1, \qquad \beta \lesssim 10^{-2}, \qquad 5 \times 10^7 \lesssim \kappa \lesssim 5 \times 10^{10},$$

with the lower values for α and β applying at the maximum extent of the temperate ice region and the upper values applying at the edges. Neglecting $\alpha \partial p_e^*/\partial z^*$, (A1)–(A2) yield the dimensionless form of (30):

$$\phi = \left(\frac{1 - z^*}{\kappa} \right)^{1/\nu}, \qquad p_e^* = \beta \left(\frac{\kappa}{1 - z^*} \right)^{1/\nu}. \tag{A3}$$

Appendix B: Extended Model

Here we present an extended model for the energy equation and the velocity. This model is used to confirm the results of the depth-integrated model presented in the main text and to illustrate the effect of lateral advection of ice on the temperature field. All calculations are done with a constant rate factor A.

B1. Heat Equation

In the presence of in-plane advection and diffusion, the energy equation is

$$\rho c_p \left(v \frac{\partial T}{\partial y} + w \frac{\partial T}{\partial z} \right) - k \nabla^2 T = \psi \qquad \text{for } T \leq T_m, \ \phi = 0, \tag{B1a}$$

where $\nabla = (\partial/\partial y, \partial/\partial z)$ operates in the $y - z$ plane. Boundary conditions have to be applied at the cold-temperate transition, at the ice surface and base, and at the lateral sides of the geometry. At the cold-temperate transition, we require continuity of mass, energy, and momentum, leading to

$$\mathbf{u}|^+ = \mathbf{u}|^-, \quad T|^+ = T|^-, \quad \left[\tau_{ij}n_j - p\delta_{ij}\right]^+ n_j = \left[\tau_{ij}n_j - p\delta_{ij}\right]^- n_j, -k\nabla T|^- \cdot \hat{\mathbf{n}} = 0. \tag{B2a}$$

The other boundary conditions remain unchanged.

Typically, models for ice stream shear margins take both lateral and vertical shear in the heat dissipation term into account (e.g., Haseloff et al., 2015, 2018; Jacobson & Raymond, 1998; Perol et al., 2015; Suckale et al., 2014):

$$\psi = \frac{A^{-1/n}}{2^{1/n}} \left(\left| \frac{\partial u}{\partial y} \right|^2 + \left| \frac{\partial u}{\partial z} \right|^2 \right)^{\frac{1+n}{2n}}. \tag{B3}$$

Including the vertical strain rate $\partial u/\partial z$ requires us to extend the model for the downstream velocity.

B2. Downstream Velocity and Heat Dissipation

In a depth-resolving model, u is determined from

$$\frac{\partial}{\partial y} \left(\eta \frac{\partial u}{\partial y} \right) + \frac{\partial}{\partial z} \left(\eta \frac{\partial u}{\partial z} \right) = -\rho g \sin \alpha \tag{B4}$$

with the viscosity

$$\eta = \frac{A^{-1/n}}{2^{1/n}} \left[\left| \frac{\partial u}{\partial y} \right|^2 + \left| \frac{\partial u}{\partial z} \right|^2 \right]^{\frac{1-n}{2n}}. \tag{B5}$$

The basal boundary conditions (8) are replaced by

$$\tau_{xz} = \tau_c \frac{u}{|u|}, \quad |u| > 0, \qquad \text{for} \quad |y| < W_m, \ z = 0,$$

$$|\tau_{xz}| \leq \tau_c, \quad u = 0, \qquad \text{for} \quad W_m < |y| < W, \ z = 0.$$

Note that the viscosity (B5) and heat dissipation (B3) only include contributions of the downstream velocity u. An analysis of the scales in ice streams and their margins shows that the other contributions are negligible (Haseloff et al., 2015).

B3. In-Plane Velocities

For a flat bed, we can integrate (2) to obtain for the ice thickness

$$H = \begin{cases} H_c = \text{const.} & \text{for} \quad |y| \leq W_s \\ \left[H_c^{2+2/n} + 2 \left[\frac{(n+2)\dot{a}}{2\bar{A}_0(\rho g)^n} \right]^{1/n} \left[(W - W_s)^{1+1/n} - (W - |y|)^{1+1/n} \right] \right]^{n/(2n+2)} & \text{for} \quad W_s \leq |y| \leq W. \end{cases}$$

For the purpose of inclusion in the heat equation, we adopt the following approximations to the velocity field, consistent with the above expression for the ice thickness:

$$u = \begin{cases} u_c \left[1 - \left(\frac{|y|}{W_s} \right)^{n+1} \right] & \text{for } |y| \leq W_s \\ 0 & \text{for } W_s \leq |y| \leq W. \end{cases}$$

Assuming $w = 0$ at $z = z_b$ and $w = -\dot{a}$ at $z = z_b + H$, the steady-state depth-integrated mass conservation is

$$\frac{\partial}{\partial y} (H\bar{v}) = \dot{a} - \frac{\partial}{\partial x} (Hu), \tag{B6}$$

where $\bar{v}$ is the depth-averaged across-stream velocity. The lateral boundary conditions are

$$\bar{v} = 0 \qquad \text{at } y = 0, \pm W.$$

From (B6), we obtain

$$\bar{v}(y) = \frac{\dot{a}}{H} \begin{cases} y - y\dfrac{W}{W_s}\dfrac{n+2}{n+1}\left[1 - \dfrac{1}{n+2}\left(\dfrac{|y|}{W_s}\right)^{n+1}\right] & \text{for } |y| \le W_s \\[2ex] -(W - |y|)\dfrac{y}{|y|} & \text{for } W_s \le |y| \le W. \end{cases}$$

In the ice stream, we have $v = \bar{v}$. In the ice ridge, we assume a shallow ice profile for v (consistent with our geometric assumptions), so that we obtain

$$v = \begin{cases} \bar{v} & \text{for } |y| \le W_s \\[2ex] \bar{v}\dfrac{(n+2)}{(n+1)}\left[1 - \left(1 - \dfrac{z}{H}\right)^{n+1}\right] & \text{for } W_s \le |y| \le W. \end{cases} \tag{B7}$$

Given u and v, we can determine w from integrating the mass balance equation ($\nabla \cdot \mathbf{u} = 0$). This yields

$$w = -\dot{a} \begin{cases} \zeta & \text{for } |y| \le W_s \\[2ex] \dfrac{n+2}{n+1}\left[\zeta - \dfrac{[1 - (1-\zeta)^{n+2}]}{n+2}\right] + \dfrac{n+2}{n+1}\left[\dfrac{(n+2)}{2\bar{A}_0(\rho g)^n}\right]^{1/n}\dfrac{\dot{a}^{1/n}}{H^{2+2/n}}(W - |y|)^{1+1/n}\zeta\left[1 - (1-\zeta)^{n+1}\right], \\ \qquad\qquad \text{for } W_s \le |y| \le W \end{cases} \tag{B8}$$

with $\zeta = z/H(y)$. v and w are discontinuous at $|y| = W_s$. To obtain smooth velocity profiles, we define the first and second cases of (B7) and (B8) as v_s, v_r, and w_s, w_r, respectively (for "stream" and "ridge"), and interpolate by writing

$$v = fv_r + (1 - f)v_s \qquad \text{and} \qquad w = fw_r + (1 - f)w_s \tag{B9}$$

with

$$f = \begin{cases} 0 & \text{for } |y| \le W_s \\[2ex] \dfrac{|y| - W_s}{W_m - W_s} & \text{for } W_s \le |y| \le W_m \\[2ex] 1 & \text{for } |y| \ge W_m. \end{cases}$$

W_m is the location of sliding onset.

References

Alley, R. B. (1989). Water-pressure coupling of sliding and bed deformation: I. Water system. *Journal of Glaciology*, *35*(119), 108–118. https://doi.org/10.3189/002214389793701527

Alley, R. B., & Bentley, C. R. (1988). Ice-core analysis on the Siple Coast of West Antarctica. *Annals of Glaciology*, *11*, 17. https://doi.org/10.3189/S0260305500006236

Alley, R. B., Blankenship, D. D., Bentley, C. R., & Rooney, S. T. (1986). Deformation of till beneath ice stream B, West Antarctica. *Nature*, *322*, 57–59. https://doi.org/10.1038/322057a0

Aschwanden, A., Bueler, E., Khroulev, C., & Blatter, H. (2012). An enthalpy formulation for glaciers and ice sheets. *Journal of Glaciology*, *58*, 441–457. https://doi.org/10.3189/2012JoG11J088

Beem, L. H., Jezek, K. C., & van der Veen, C. J. (2010). Basal melt rates beneath Whillans Ice Stream, West Antarctica. *Journal of Glaciology*, *56*, 647–654. https://doi.org/10.3189/002214310793146241

Blankenship, D. D., Bentley, C. R., Rooney, S. T., & Alley, R. B. (1986). Seismic measurements reveal a saturated porous layer beneath an active Antarctic ice stream. *Nature*, *322*, 54–57. https://doi.org/10.1038/322054a0

Blankenship, D. D., Bentley, C. R., Rooney, S. T., & Alley, R. B. (1987). Till beneath ice stream B. I—Properties derived from seismic travel times. II—Structure and continuity. III—Till deformation—Evidence and implications. IV—A coupled ice-till flow model. *Journal of Geophysical Research*, *92*, 8903–8940. https://doi.org/10.1029/JB092iB09p08903

Bougamont, M., Tulaczyk, S., & Joughin, I. (2003). Numerical investigations of the slow-down of Whillans Ice Stream, West Antarctica: Is it shutting down like Ice Stream C? *Annals of Glaciology*, *37*, 239–246. https://doi.org/10.3189/172756403781815555

Catania, G., Hulbe, C., Conway, H., Scambos, T. A., & Raymond, C. F. (2012). Variability in the mass flux of the Ross ice streams, West Antarctica, over the last millennium. *Journal of Glaciology*, *58*, 741–752. https://doi.org/10.3189/2012JoG11J219

Catania, G. A., Scambos, T. A., Conway, H., & Raymond, C. F. (2006). Sequential stagnation of Kamb Ice Stream, West Antarctica. *Geophysical Research Letters*, *33*, L14502. https://doi.org/10.1029/2006GL026430

Christoffersen, P., Bougamont, M., Carter, S. P., Fricker, H. A., & Tulaczyk, S. (2014). Significant groundwater contribution to Antarctic ice streams hydrologic budget. *Geophysical Research Letters*, *41*, 2003–2010. https://doi.org/10.1002/2014GL059250

Conway, H., Catania, G., Raymond, C. F., Gades, A. M., Scambos, T. A., & Engelhardt, H. (2002). Switch of flow direction in an Antarctic ice stream. *Nature*, *419*, 465–467. https://doi.org/10.1038/nature01081

Cuffey, K. M., & Paterson, W. S. B. (2010). *The physics of glaciers*. Amsterdam: Butterworth-Heinemann/Elsevier. ISBN: 9780123694614.

Duval, P. (1977). The role of the water content on the creep rate of polycrystalline ice, Symposium at Grenoble 1975 - Isotopes and Impurities in Snow and Ice, IAHS Publ. (Vol. 118, pp. 29–33), Red Books. Oxfordshire OX10 8BB, UK: IAHS, CEH Wallingford.

Echelmeyer, K. A., & Harrison, W. D. (1999). Ongoing margin migration of Ice Stream B, Antarctica. *Journal of Glaciology*, *45*(150), 361–369. https://doi.org/10.3189/S0022143000001866

Echelmeyer, K. A., Harrison, W. D., Larsen, C., & Mitchell, J. E. (1994). The role of the margins in the dynamics of an active ice stream. *Journal of Glaciology*, *40*, 527–538. https://doi.org/10.3189/S0022143000012417

Elsworth, C. W., & Suckale, J. (2016). Rapid ice flow rearrangement induced by subglacial drainage in West Antarctica. *Geophysical Research Letters*, *43*, 11–697. https://doi.org/10.1002/2016GL070430

Engelhardt, H., Humphrey, N., Kamb, B., & Fahnestock, M. (1990). Physical conditions at the base of a fast moving Antarctic ice stream. *Science*, *248*, 57–59. https://doi.org/10.1126/science.248.4951.57

Engelhardt, H., & Kamb, B. (1997). Basal hydraulic system of a West Antarctic ice stream: Constraints from borehole observations. *Journal of Glaciology*, *43*, 207–230. https://doi.org/10.3189/S0022143000003166

Fahnestock, M. A., Scambos, T. A., Bindschadler, R. A., & Kvaran, G. (2000). A millennium of variable ice flow recorded by the Ross Ice Shelf, Antarctica. *Journal of Glaciology*, *46*, 652–664. https://doi.org/10.3189/172756500781832693

Flowers, G. E. (2015). Modelling water flow under glaciers and ice sheets. *Proceedings of the Royal Society of London A: Mathematical, Physical and Engineering Sciences*, *471*(2176), 20140907. https://doi.org/10.1098/rspa.2014.0907

Fowler, A. C. (1984). On the transport of moisture in polythermal glaciers. *Geophysical and Astrophysical Fluid Dynamics*, *28*, 99–140. https://doi.org/10.1080/03091928408222846

Fretwell, P., Pritchard, H. D., Vaughan, D. G., Bamber, J. L., Barrand, N. E., Bell, R., et al. (2013). Bedmap2: Improved ice bed, surface and thickness datasets for Antarctica. *The Cryosphere*, *7*(1), 375–393. https://doi.org/10.5194/tc-7-375-2013

Fricker, H. A., Scambos, T., Bindschadler, R., & Padman, L. (2007). An active subglacial water system in West Antarctica mapped from space. *Science*, *315*, 1544–1548. https://doi.org/10.1126/science.1136897

Gagliardini, O., Zwinger, T., Gillet-Chaulet, F., Durand, G., Favier, L., Fleurian, B. d., et al. (2013). Capabilities and performance of Elmer/Ice, a new generation ice-sheet model. *Geoscientific Model Development*, *6*, 1299–1318. https://doi.org/10.5194/gmd-6-1299-2013

Goldsby, D. L., & Kohlstedt, D. L. (2001). Superplastic deformation of ice: Experimental observations. *Journal of Geophysical Research*, *106*(B6), 11,017–11,030. https://doi.org/10.1029/2000JB900336

Gray, L., Joughin, I., Tulaczyk, S., Spikes, V. B., Bindschadler, R., & Jezek, K. (2005). Evidence for subglacial water transport in the West Antarctic Ice Sheet through three-dimensional satellite radar interferometry. *Geophysical Research Letters*, *32*, L03501. https://doi.org/10.1029/2004GL021387

Greene, C. A., Gwyther, D. E., & Blankenship, D. D. (2017). Antarctic Mapping Tools for Matlab. *Computers & Geosciences*, *104*, 151–157. https://doi.org/10.1016/j.cageo.2016.08.003

Greve, R. (1997). A continuum-mechanical formulation for shallow polythermal ice sheets. *Philosophical Transactions of the Royal Society of London. Series A: Mathematical, Physical and Engineering Sciences*, *355*(1726), 921–974. https://doi.org/10.1098/rsta.1997.0050

Hamilton, G. S., Whillans, I. M., & Morgan, P. J. (1998). First point measurements of ice-sheet thickness change in Antarctica. *Annals of Glaciology*, *27*, 125–129. https://doi.org/10.3189/1998AoG27-1-125-129

Haseloff, M., Schoof, C., & Gagliardini, O. (2015). A boundary layer model for ice stream margins. *Journal of Fluid Mechanics*, *781*, 353–387. https://doi.org/10.1017/jfm.2015.503

Haseloff, M., Schoof, C., & Gagliardini, O. (2018). The role of subtemperate slip in thermally driven ice stream margin migration. *The Cryosphere*, *12*, 2545–2568. https://doi.org/10.5194/tc-12-2545-2018

Hewitt, I. J. (2011). Modelling distributed and channelized subglacial drainage: The spacing of channels. *Journal of Glaciology*, *57*(202), 302–314. https://doi.org/10.3189/002214311796405951

Hewitt, I. J., & Schoof, C. (2017). Models for polythermal ice sheets and glaciers. *The Cryosphere*, *11*(1), 541–551. https://doi.org/10.5194/tc-11-541-2017

Hulbe, C., & Fahnestock, M. (2007). Century-scale discharge stagnation and reactivation of the Ross ice streams, West Antarctica. *Journal of Geophysical Research*, *112*, F03S27. https://doi.org/10.1029/2006JF000603

Hutter, K. (1983). *Theoretical glaciology*. Netherlands: D. Reidel Publishing Company/ Terra Scientific Publishing Company.

Jacobson, H. P., & Raymond, C. F. (1998). Thermal effects on the location of ice stream margins. *Journal of Geophysical Research*, *103*, 12,111–12,122. https://doi.org/10.1029/98JB00574

Jordan, R. E., & Stark, J. A. (2001). Capillary tension in rotting ice layers (*ERDC/CRREL TR-01-13*). NTIS, 5285 Port Royal Rd, Springfield VA 22161: Cold Regions Research and Engineering Laboratory.

Kamb, B. (2001). Basal zone of the West Antarctic ice streams and its role in lubrication of their rapid motion. In R. B. Alley, & R. A. Bindschadler (Eds.), *The West Antarctic Ice Sheet: Behaviour and Environment, Antarctic Research Series* (Vol. 77, pp. 157–199). Washington: American Geophysical Union.

Kyrke-Smith, T. M., Katz, R. F., & Fowler, A. C. (2014). Subglacial hydrology and the formation of ice streams. *Proceedings of the Royal Society A: Mathematical, Physical and Engineering Science*, *470*(2161), 20130494. https://doi.org/10.1098/rspa.2013.0494

Kyrke-Smith, T. M., Katz, R. F., & Fowler, A. C. (2015). Subglacial hydrology as a control on emergence, scale, and spacing of ice streams. *Journal of Geophysical Research: Earth Surface*, *120*, 1501–1514. https://doi.org/10.1002/2015JF003505

Leeman, J. R., Valdez, R. D., Alley, R. B., Anandakrishnan, S., & Saffer, D. M. (2016). Mechanical and hydrologic properties of Whillans Ice Stream till: Implications for basal strength and stick-slip failure. *Journal of Geophysical Research: Earth Surface*, *121*, 1295–1309. https://doi.org/10.1002/2016JF003863

Lingle, C. S., & Brown, T. J. (1987). A subglacial aquifer bed model and water pressure dependent basal sliding relationship for a West Antarctic ice stream, *Dynamics of the West Antarctic ice sheet* (pp. 249-285). Dordrecht: Springer.

Lliboutry, L. (1968). General theory of subglacial cavitation and sliding of temperate glaciers. *Journal of Glaciology*, *7*(49), 21–58. https://doi.org/10.3189/S0022143000020396

MacAyeal, D. R. (1989). Large-scale ice flow over a viscous basal sediment—Theory and application to ice stream B, Antarctica. *Journal of Geophysical Research*, *94*, 4071–4087. https://doi.org/10.1029/JB094iB04p04071

Matsuoka, K., Skoglund, A., & Roth, G. (2018). Quantarctica. Norwegian Polar Institute, https://doi.org/10.21334/npolar.2018.8516e961

McKenzie, D. (1984). The generation and compaction of partially molten rock. *Journal of Petrology*, *25*(3), 713–765. https://doi.org/10.1093/petrology/25.3.713

Meyer, C. R., & Minchew, B. M. (2018). Temperate ice in the shear margins of the Antarctic Ice Sheet: Controlling processes and preliminary locations. *Earth and Planetary Science Letters*, *498*, 17–26. https://doi.org/10.1016/j.epsl.2018.06.028

Meyer, C. R., Yehya, A., Minchew, B., & Rice, J. R. (2018). A model for the downstream evolution of temperate ice and subglacial hydrology along ice stream shear margins. *Journal of Geophysical Research: Earth Surface*, *123*, 1682–1698. https://doi.org/10.1029/2018JF004669

Minchew, B. M., Meyer, C. R., Robel, A. A., Gudmundsson, G. H., & Simons, M. (2018). Processes controlling the downstream evolution of ice rheology in glacier shear margins: Case study on Rutford Ice Stream, West Antarctica. *Journal of Glaciology*, *64*, 112. https://doi.org/10.1017/jog.2018.47

Morland, L. W., & Johnson, I. R. (1980). Steady motion of ice sheets. *Journal of Glaciology*, *25*(92), 229–246. https://doi.org/10.3189/S0022143000010467

Muszynski, I., & Birchfield, G. E. (1987). A coupled marine ice-stream-ice-shelf model. *Journal of Glaciology*, *33*(113), 3–15. https://doi.org/10.3189/S0022143000005281

Nye, J. F. (1976). Water flow in glaciers: Jökulhlaups, tunnels and veins. *Journal of Glaciology*, *17*(76), 181207. https://doi.org/10.3189/S002214300001354X

Nye, J. F., & Frank, F. C. (1973). Hydrology of the Intergranular veins in a temperate glacier, *Cambridge Symposium, 1969, Hydrology of Glaciers* (Vol. 95, pp. 157–161). Oxfordshire OX10 8BB, UK: IAHS: CEH Wallingford.

Perol, T., & Rice, J. R. (2015). Shear heating and weakening of the margins of West Antarctic ice streams. *Geophysical Research Letters*, *42*, 3406–3413. https://doi.org/10.1002/2015GL063638

Perol, T., Rice, J. R., Platt, J. D., & Suckale, J. (2015). Subglacial hydrology and ice stream margin locations. *Journal of Geophysical Research: Earth Surface*, *120*, 1352–1368. https://doi.org/10.1002/2015JF003542

Platt, J. D., Perol, T., Suckale, J., & Rice, J. R. (2016). Determining conditions that allow a shear margin to coincide with a Röthlisberger channel. *Journal of Geophysical Research: Earth Surface*, *121*, 1273–1294. https://doi.org/10.1002/2015JF003707

Raymond, C. (1996). Shear margins in glaciers and ice sheets. *Journal of Glaciology*, *42*, 90–102. https://doi.org/10.3189/S0022143000030550

Raymond, C. F. (2000). Energy balance of ice streams. *Journal of Glaciology*, *46*, 665–674. https://doi.org/10.3189/172756500781832701

Retzlaff, R., & Bentley, C. R. (1993). Timing of stagnation of Ice Stream C, West Antarctica, from short-pulse radar studies of buried surface crevasses. *Journal of Glaciology*, *39*(133), 553–561. https://doi.org/10.3189/S0022143000016440

Rignot, E., Mouginot, J., & Scheuchl, B. (2011). Ice flow of the Antarctic Ice Sheet. *Science*, *333*(6048), 1427–1430. https://doi.org/10.1126/science.1208336

Rignot, E., Mouginot, J., & Scheuchl, B. (2017). MEaSUREs InSAR-based Antarctica ice velocity map, Version 2. https://doi.org/10.5067/D7GK8F5J8M8R

Röthlisberger, H. (1972). Water pressure in subglacial channels. *Journal of Glaciology*, *11*(62), 177–203. https://doi.org/10.3189/S0022143000022188

Rudge, J. F. (2018). Textural equilibrium melt geometries around tetrakaidecahedral grains. *Proceedings of the Royal Society of London A: Mathematical, Physical and Engineering Sciences*, *474*(2212), 20170639. https://doi.org/10.1098/rspa.2017.0639

Schoof, C. (2004). On the mechanics of ice-stream shear margins. *Journal of Glaciology*, *50*, 208–218. https://doi.org/10.3189/172756504781830024

Schoof, C. (2006). A variational approach to ice stream flow. *Journal of Fluid Mechanics*, *556*, 227–251. https://doi.org/10.1017/S0022112006009591

Schoof, C. (2012). Thermally driven migration of ice-stream shear margins. *Journal of Fluid Mechanics*, *712*, 552–578. https://doi.org/10.1017/jfm.2012.438

Schoof, C., & Hewitt, I. J. (2016). A model for polythermal ice incorporating gravity-driven moisture transport. *Journal of Fluid Mechanics*, *797*, 504–535. https://doi.org/10.1017/jfm.2016.251

Spiegelman, M. (1993). Flow in deformable porous media. Part 1 Simple analysis. *Journal of Fluid Mechanics*, *247*(1), 17–38. https://doi.org/10.1017/S0022112093000369

Stearns, L. A., Jezek, K. C., & Van der Veen, C. J. (2005). Decadal-scale variations in ice flow along Whillans Ice Stream and its tributaries, West Antarctica. *Journal of Glaciology*, *51*(172), 147–157. https://doi.org/10.3189/172756505781829610

Stephenson, S. N., & Bindschadler, R. A. (1988). Observed velocity fluctuations on a major Antarctic ice stream. *Nature*, *334*, 695–697. https://doi.org/10.1038/334695a0

Suckale, J., Platt, J. D., Perol, T., & Rice, J. R. (2014). Deformation-induced melting in the margins of the West Antarctic ice streams. *Journal of Geophysical Research: Earth Surface*, *119*, 1004–1025. https://doi.org/10.1002/2013JF003008

Tulaczyk, S., Kamb, W. B., & Engelhardt, H. F. (2000a). Basal mechanics of Ice Stream B, West Antarctica II. Plastic-undrained-bed-model. *Journal of Geophysical Research*, *105*, 463–482. https://doi.org/10.1029/1999JB900329

Tulaczyk, S., Kamb, W. B., & Engelhardt, H. F. (2000b). Basal mechanics of Ice Stream B, West Antarctica I. Till mechanics. *Journal of Geophysical Research*, *105*, 463–482. https://doi.org/10.1029/1999JB900329

Walder, J. S. (1986). Hydraulics of subglacial cavities. *Journal of Glaciology*, *32*(112), 439–445. https://doi.org/10.3189/S0022143000012156

Walder, J. S., & Fowler, A. (1994). Channelized subglacial drainage over a deformable bed. *Journal of Glaciology*, *40*(134), 3–15. https://doi.org/10.3189/S0022143000003750